Optical Materials: X 12 (2021) 100118

Contents lists available at ScienceDirect

Optical Materials: X

journal homepage: www.journals.elsevier.com/optical-materials-x

Invited Article

Synthesis and characterization of Nd^{3+}-Yb^{3+} doped hydroxyapatite nanoparticles

Marco Vittorio Nardi [a,*], Melanie Timpel [a], Enrico Biondani [b], Riccardo Ceccato [b], Andrea Chiappini [c], Sandra Dirè [b]

[a] IMEM-CNR Institute of Materials for Electronics and Magnetism, Trento Unit C/o Fondazione Bruno Kessler, Via Alla Cascata 56/C, Povo, 38123, Trento, Italy
[b] Department of Industrial Engineering, University of Trento, Via Sommarive 9, Povo, 38123, Trento, Italy
[c] CNR-IFN, CSMFO Lab & FBK Photonics Unit, Via Alla Cascata 56/C, Povo, 38123, Trento, Italy

ARTICLE INFO

Keywords:
Hydroxyapatite nanoparticles
Lanthanide doping
Nd^{3+}-Yb^{3+} energy transfer
Down-shifting

ABSTRACT

The present work focuses on Nd^{3+}-Yb^{3+} co-doping of bare and Sr-substituted hydroxyapatite nanoparticles and their chemical, structural and optical characterization. An energy transfer between Nd^{3+} and Yb^{3+} centers was found, generating an efficient down-shifting process, where Nd^{3+} absorbs at a low near-infrared wavelength and Yb^{3+} emits at its characteristic $^2F_{7/2} \rightarrow {}^2F_{5/2}$ transition. The energy transfer was found to be more efficient in Sr-substituted than in bare hydroxyapatite nanoparticles. The synthesized Nd^{3+}-Yb^{3+} doped hydroxyapatite nanoparticles can potentially find applications not only as diagnostic near-infrared down-shifting agent but also as nanosystem for near-infrared photoactivated treatment.

1. Introduction

Light-responsive nanoparticles (NPs) play a key role in biomedical applications for diagnostics, imaging, targeted therapy and in medical devices to sustain and improve human health [1], and may even be used as local light sources for disinfection of reusable, wearable protective equipment [2]. Some major obstacles for their biomedical use is their often limited biocompatibility [3] as well as the response of human tissue on light by itself, which can lead to serious overheating effects and tissue damage [4–6]. In this context, developing a class of nanomaterials with the desired biocompatibility and allowing an internal energy transfer to adjust the excitation window to lower excitation windows in the near-infrared (NIR) region, where human tissue absorption, damage and autofluorescence is reduced, is of large interest for the biophysics and biomedical community.

Within the wide range of materials that demonstrate to be highly biocompatible, hydroxyapatite (HA) has been already used in numerous applications ranging from bone tissue repair and regeneration, in forms of scaffolds or coupled with polymer or ceramic materials for dental implants and bio-coatings [7]. In addition to the well-known biocompatibility, the HA structure makes it a suitable candidate to transfer or add specific functionalities via chemical-structural modifications [8] and thus to engineer its optical properties.

In the last years, attention has been drawn to doping of HA nanoparticles (NPs) with lanthanides for various biomedical applications [9–11], while other inorganic NPs such as $NaYF_4$ and $NaGdF_4$ have been co-doped with Nd^{3+}-Yb^{3+} extending the excitation of the NPs to shorter NIR wavelengths [12,13].

More specifically, the Yb^{3+} ion absorbs NIR light at ~980 nm and can be easily excited with common lasers, according to its $^2F_{7/2} \rightarrow {}^2F_{5/2}$ transition [4]. Nevertheless, dealing with biological applications, the Yb^{3+} absorption peak at 980 nm overlaps with the maximum absorption band of water molecules. This results in the attenuation of the effective incident laser power, leading to the decrease of penetration depth in human tissue, but also to possible damage to cells and tissues due to significant rise in temperature [4,5]. Since absorption by water decreases significantly at lower wavelengths, an excitation at around 800 nm is a valid solution for deep tissue applications with less tissue overheating. In order to obtain a strong and stable luminescent emission under the excitation at 800 nm, Nd^{3+} was found to be a good option as energy donor along with Yb^{3+} as energy acceptor [12,13], allowing an effective energy transfer (ET) between the two centers [14].

In the present study, Nd^{3+} and Yb^{3+} were chosen as dopants for HA and Sr-substituted (75 mol.% Sr) HA NPs. The latter HA matrix has been previously found to be the optimal composition for the cells viability and proliferation [15]. The NPs were synthesized via an aqueous

* Corresponding author.
E-mail address: marcovittorio.nardi@imem.cnr.it (M.V. Nardi).

https://doi.org/10.1016/j.omx.2021.100118
Received 3 November 2021; Received in revised form 11 November 2021; Accepted 13 November 2021
Available online 23 November 2021

precipitation method [16] using two different Nd^{3+} and Yb^{3+} amounts (1.5 and 2 mol.%). The influence of Sr substitution and lanthanide doping on the HA NPs with respect to their structural and morphological properties was studied. Moreover, the emission properties of the Nd^{3+}-Yb^{3+} doped NPs (both bare HA and Sr-HA) were investigated, highlighting effective energy transfer from the Nd^{3+} ions used as absorber to the one used as emitter (i.e., Yb^{3+}).

2. Materials and methods

2.1. Synthesis of HA nanoparticles

Hydroxyapatite (HA) and Sr-substituted HA nanopowders were synthetized by chemical precipitation in aqueous media [15,16]. Two main compositions were studied, namely pure calcium HA (in the following denoted as Ca100) and HA powders with 75 mol% of Sr^{2+} replacing Ca^{2+} into the apatite structure (Sr75).

An aqueous $(NH_4)HPO_4$ solution (50 ml, 0.65 M) was prepared as P-source (ammonium phosphate dibasic $\geq$ 98 wt%, Sigma-Aldrich), whereas the Ca-source was an aqueous solution (50 ml, 1.08 M) of calcium nitrate tetrahydrate [$Ca(NO_3)_2 \cdot H_2O$, $\geq$ 99 wt%, Sigma-Aldrich]. Anhydrous strontium nitrate [$Sr(NO_3)_2$, $\geq$ 99 wt%, Sigma-Aldrich] was added to the calcium nitrate solution for the synthesis of Sr-substituted HA powders.

Besides undoped HA (Ca100 and Sr75), Nd^{3+}-Yb^{3+} doped HA NPs with different concentrations of lanthanide ions (xYb:xNd:Ca100 and xYb:xNd:Sr75; x = 1.5, 2) were synthesized by adding neodymium (III) nitrate hexahydrate [$Nd(NO_3)_3 \cdot 6H_2O$, $\geq$ 99.9 wt%, Aldrich chemistry] and ytterbium (III) nitrate pentahydrate [$Yb(NO_3) \cdot 5H_2O$, $\geq$ 99.9 wt%, Aldrich chemistry]. Furthermore, a reference sample without Nd^{3+} doping was synthesized, namely 1.5 Yb:Ca100.

With respect to pure Ca-HA (Ca100), the contents of Sr, Nd and Yb in the final powders were adjusted by varying the relative amounts of nitrates [$Ca(NO_3)_2 \cdot H_2O$, $Sr(NO_3)_2$, $Nd(NO_3)_3 \cdot 6H_2O$ and $Yb(NO_3) \cdot 5H_2O$] in the solution. The pH of the solutions was adjusted to 10 by adding concentrated ammonia solution (NH_4OH, 28–30 vol%, J.T. Baker) in order to improve the crystallinity and purity of the synthesized HA NPs [17].

The nitrate solutions (adjusted at pH = 10) were placed in a two-necked reaction flask equipped with a reflux condenser and kept under nitrogen flow in order to prevent any HA carbonatation. The ammonium phosphate solution was poured in a dropping funnel provided with a by-pass. The two-necked-flask was immersed into a silicon oil bath, previously heated up to 90 °C by a heating plate. After 10 min, the ammonium phosphate solution (adjusted at pH 10) was added to the nitrate solution with a dropping rate of around 1.5 ml/min. The reaction was allowed to continue for 5 h at 90 °C under vigorous stirring and static nitrogen conditions. Once it was completed, the product appeared in the form of a white slurry. The powders were separated by centrifugation for 10 min at 8000 rpm and repeatedly washed and centrifugated several times until the washing solution showed pH ~7.

2.2. Characterization

Inductively coupled plasma optical emission spectroscopy (ICP-OES) was used with an Ametek spectrometer (Spectro Ciros Vision CCD, 125–770 [nm]) for the determination of purity and chemical composition of the synthetized powders. The reagents used for standards and samples were hydroxyapatite ultrapure standard (>99.995% trace metal basis, reagent-grade, Sigma-Aldrich), 1 g/l Sr standard (BHD Spectrosol), Yb standard and Nd standard. Moreover, ultrapure nitric acid (70 vol%, Aldrich) was used for dissolving the samples. In addition, since Sr easily ionizes, Cs was utilized as ionizing suppressor, as it has a stronger ionization tendency compared to Sr. In this way, the ionizing conditions were uniformed.

Fourier transform infrared spectroscopy (FTIR) analyses were performed with an Avatar 330 Thermo FTIR spectrometer on KBr pellets in transmission mode within the range 4000–400 cm^{-1}, collecting 64 scans with a resolution of 4 cm^{-1}.

X-ray diffraction (XRD) was carried out to analyze the phase composition of the powders, along with a structural characterization. A Rigaku DMAX III 4057A2 Bragg Brentano powder diffractometer with Cu source (Kα radiation = 1.54056 Å) was used, operating at 40 kV and 30 mA with a curved graphite monochromator in the diffracted beam. The data were collected in the 2θ angle range 10–60°, with step size of 0.03° and dwell time of 10 s/step. The spectra were analyzed by Jade8 (Materials Data Inc., MDI, Livermore, CA, USA) for the qualitative phase identification and by the Rietveld-based software MAUD [18] for the quantitative phase analysis and the calculation of crystallites size.

Powder size and morphology were investigated by means of a transmission electron microscope (TEM) ThermoFischer Talos™ F200S, operating at 200 kV. For TEM sample preparation, around 5 mg of powder were dissolved in acetone and sonicated for 5 min 50 μl of the resulting suspensions were then deposited on copper grids, covered by an amorphous carbon film, in order to allow solvent evaporation.

Absorbance measurements were carried out on aqueous solutions of the lanthanide precursors using a UV-VIS Jasco V-570 Spectrometer. Nd $(NO_3)_3 \cdot 6H_2O$ and $Yb(NO_3) \cdot 5H_2O$ were dissolved in pure water with a concentration of 0.045 M. The solutions were analyzed by scanning at 400 nm/min in the range between 350 and 1100 nm with a resolution of 1 nm.

The samples' photoluminescence (PL) emission was collected by exciting the materials with λ = 340 nm excitation source provided by a M340L4 UV LED diode (Thorlabs). A convex lens of 20 cm focal length was adopted to focus the excitation beam on the samples, with a nominal power output of 60 mW. The emission was detected by means of a Hamamatsu photomultiplier tube and standard lock-in technique. For the sake of comparison, all spectra were collected with the same geometry, focus, spot dimensions and detector parameters.

3. Results and discussion

3.1. Chemical composition

Table 1 shows the measured chemical composition (molar ratio) of the synthetized samples with respect to the nominal content. It is found that all samples are deficient in Sr^{2+} and Yb^{3+} ions compared to the nominal values.

The chemical composition of the synthesized samples is close to the expected nominal values. The slightly lower amount of Sr^{2+} with respect to the nominal one is in agreement with previous findings for Sr-substituted HA NPs [15].

3.2. Structural properties

Fig. 1 displays FT-IR spectra of the undoped HA NPs (Ca100 and Sr75) and corresponding Nd^{3+}-Yb^{3+} doped HA samples, i.e., xYb:xNd:Ca100 and xYb:xNd:Sr75; x = 1.5, 2. All spectra in Fig. 2 are normalized to the intensity of the most intense peak of the Ca100 sample located at

Table 1
Chemical composition of undoped and Nd^{3+}-Yb^{3+} doped HA samples as determined by ICP-OES.

	Sr^{2+}	Nd^{3+}	Yb^{3+}
sample	[mol.%]		
Ca100	0	0	0
Sr75	73.20 ± 0.57	0	0
1.5 Yb:1.5Nd:Ca100	0	1.61 ± 0.01	1.23 ± 0.01
2 Yb:2Nd:Ca100	0	2.22 ± 0.03	1.65 ± 0.01
1.5 Yb:1.5Nd:Sr75	70.82 ± 0.22	1.73 ± 0.01	1.19 ± 0.01
2 Yb:2Nd:Sr75	69.17 ± 0.42	2.27 ± 0.04	1.74 ± 0.02

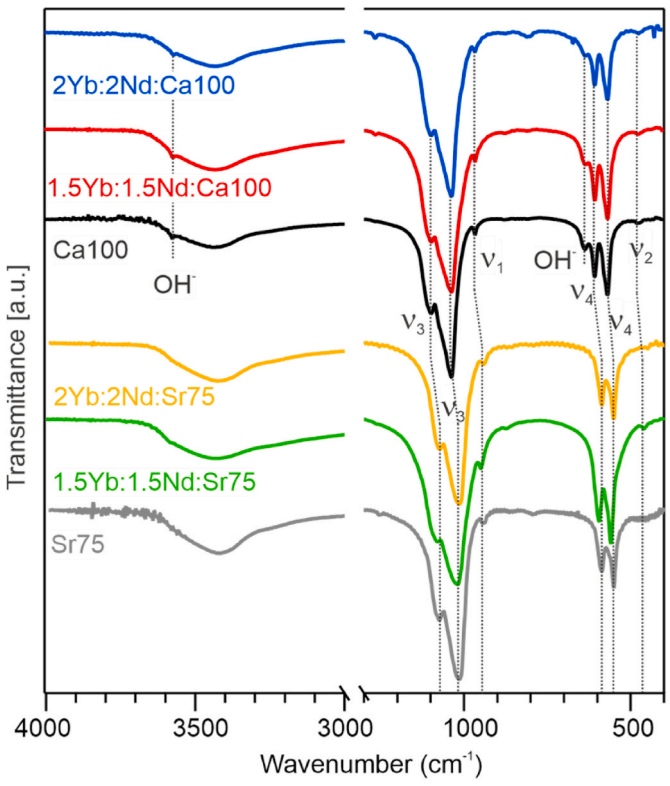

Fig. 1. FT-IR spectra of undoped (Ca100/Sr75) and Nd^{3+}-Yb^{3+} doped HA samples as indicated in the figure. The main vibrations are highlighted with labels and dashed lines.

1037 cm^{-1}.

The FT-IR spectrum of the undoped HA NPs (Ca100, black curve in Fig. 1) is in good agreement with the characteristic OH^- and PO_4^{3-} vibrations in the HA lattice as reported in literature [19,20]. The peak positions, peak labels and corresponding assignments are listed in Table 2. It is worth noting that the absence of a doublet at 1411 and 1466 cm^{-1} referred to CO_3^{2-} (spectral range not shown) as well as the absence of bands at 868, 875, 1215 and 2400 cm^{-1} due to monohydrogen phosphate HPO_4^{2-} groups [19] underlines the reliability of the present synthesis route.

After Nd^{3+}-Yb^{3+} doping (red and blue curve in Fig. 1), the typical vibrational bands related to HA are still present, exhibiting no significant band shifts. By increasing the lanthanide concentration from x = 1.5 to 2, a slight decrease in intensity for the OH^- vibrational bands is observed. According to Barralet et al. [21], this is directly connected to a decrease of particle crystallinity.

By comparing the Sr-substituted HA NPs (Sr75, gray curve in Fig. 1) with Ca100, it is evident that the characteristic OH^- vibrations are not detectable, in good agreement with previous observations of their gradual decrease with increasing Sr^{2+} concentrations [15]. An additional effect related to Sr^{2+} substitution is that all phosphate bands ν_1 – ν_4 are slightly shifted (20-24 cm^{-1}) to lower wavenumbers. Progressive red-shifts with increasing Sr^{2+} concentration have been previously reported [15], and can be related to the energy loss of some P–O bonds, due to the increase of reciprocal distance between different phosphate groups. In fact, since Sr^{2+} has a larger ionic radius than Ca^{2+}, the ionic substitution involves a lattice expansion [22] that leads to an anion separation and a decrease of the anion-anion repulsion forces [19]. Besides the band shifts, a slight broadening of the ν_3 signal is observed, and the ν_4 mode reveals two small asymmetric shoulders. These two components can be ascribed to internal PO_4^{3-} and protonated surface -HPO_x, respectively [23]. The FT-IR signals of Nd^{3+}-Yb^{3+} doped Sr-HA samples (green and orange curve in Fig. 1) are slightly broadened and an increase in intensity is registered for most phosphate bands with respect to ν_3 at ~1037 cm^{-1}.

In Fig. 2a and b, XRD patterns of undoped HA NPs (Ca100 and Sr75) are displayed in comparison with corresponding Nd^{3+}-Yb^{3+} doped HA samples. The qualitative analysis for Ca100 (Fig. 2a) results in a perfect matching with the reference of the HA crystal structure (PDF#00-009-0432), i.e., the undoped HA NPs exhibit a hexagonal crystal structure belonging to the P63=m space group, with a=b=9.418 Å, c=6.884 Å, α=β=90°, γ=120°. The presence of Nd^{3+} and Yb^{3+} ions in the Nd^{3+}-Yb^{3+} doped HA samples does not affect the crystalline features of the HA NPs (see Fig. 2a). No peak shifts can be observed, while a general broadening and a slight decrease in peak intensities are detectable, indicating a reduction of the overall NPs' crystallinity. No further peaks are found, demonstrating that neither $Yb(PO)_4$ nor $Nd(PO)_4$ are formed at concentrations up to 2 mol.% for each lanthanide.

The XRD pattern of Sr-substituted HA NPs (Sr75) in Fig. 2b shows that the hexagonal crystal structure is maintained with a=b=9.68 Å, c=7.19 Å, in good agreement with previous studies of Sr-substituted HA NPs [15]. However, the signal of Sr75 is shifted towards lower 2θ angles with respect to Ca100. A general broadening is observed, resulting in a partial overlap of some peaks. It is remarkable that the relative intensity of the (002) diffraction decreases, which may reflect an influence on the shape of the crystallites and eventually on particle size, since the HA crystal grows preferentially along the c-axis. The corresponding XRD patterns of the Nd^{3+}-Yb^{3+} doped Sr-HA samples exhibit further peak broadening and reduced intensities, in agreement with the findings for the Nd^{3+}-Yb^{3+} doped HA samples. It is worth noting that XRD results can be related to the trend observed by FT-IR analysis, namely the weakening of the OH^- stretching vibrations by increasing lanthanide concentrations, which can be explained in terms of reduced dimensions of the crystallites and decrease in intensity of the (002) diffraction peak, since OH^- groups are oriented along the c-axis of the crystalline cell.

Since the (002) plane refers to particles' c-axis, along which the crystals should preferentially grow, the decrease of XRD intensity indicates that the growth along this direction is inhibited. This result is consistent with the dimension of crystalline domains, that turns out to be maximum for Ca100 and decreases due to Sr^{2+} substitution and Nd^{3+}/Yb^{3+} doping.

Fig. 2c–f) shows the morphology of the NPs of undoped Ca100 and Sr75 samples (Fig. 2c,e) and the corresponding Nd^{3+}-Yb^{3+} doped samples (Fig. 2d,f) with 2 mol.% Yb^{3+} and Nd^{3+} (i.e., 2 Yb:2Nd:Ca100 and 2 Yb:2Nd:Sr75). All HA NPs are characterized by a hexagonal rod-like shape, with a broad distribution of their length. The average particle length and width is reported in Table 3. The largest structures (major axis around 150 nm) were observed in the Ca100 sample. The rod-like NPs tend to get shorter and thinner due to Ca-to-Sr substitution, while lanthanide doping results in a further decrease in length, along with an additional broadening of the size distribution.

3.3. Optical properties

Fig. 3a shows the absorbance spectra of $Yb(NO_3)_3$ and $Nd(NO_3)_3$ aqueous solutions (0.045 M). The spectrum measured for $Yb(NO_3)_3$ exhibits a broad band at 970 nm with a small shoulder at 935 nm, corresponding to the $^2F_{5/2}$ excited state of Yb^{3+} [24]. The $Nd(NO_3)_3$ spectrum is characterized by a wide range of possible excitation bands, that can be obtained exciting from the $^4I_{9/2}$ ground state. In order to proof efficient energy transfer between Nd and Yb, the Nd^{3+} centers were excited at 340 nm, in order to be close to the absorption band of the Nd^{3+} at around 350 nm and far away from any absorption bands of the Yb^{3+} ion.

The PL emission spectra of undoped and Nd^{3+}-Yb^{3+} doped HA and Sr-HA NPs are reported in Fig. 3b. No emission is detected for the undoped Ca100 sample (black curve). For the reference sample without Nd^{3+} ions, i.e., 1.5 Yb:Ca100 (blue curve), a slight emission is measured at 980 nm even if there is no direct absorbance by Yb^{3+}. This can be

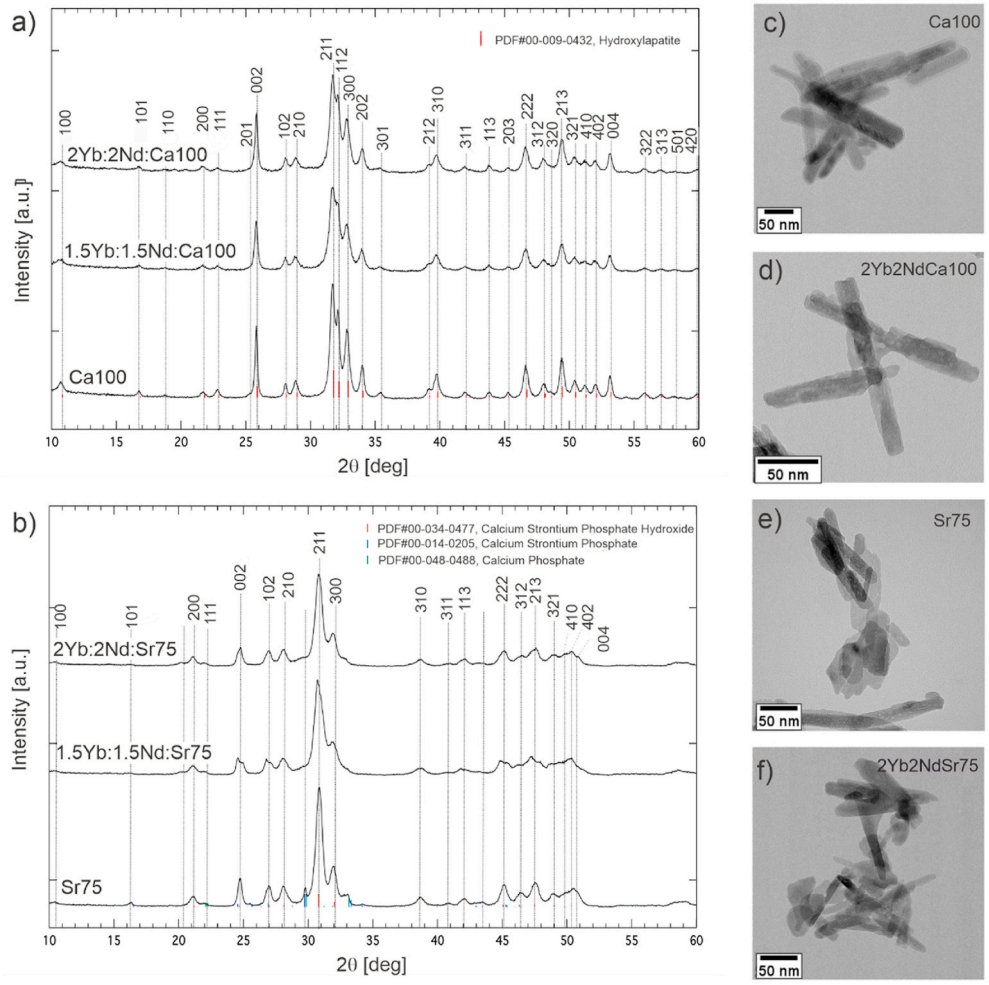

Fig. 2. (a, b) XRD pattern of (a) Ca100 and xYb:xNd:Ca100 samples, and (b) Sr75 and xYb:xNd:Sr75 samples; (c–f) TEM bright field images of undoped and Nd^{3+}-Yb^{3+} doped HA samples.

Table 2
Assignment of vibrational modes as measured by FI-IR for the Ca100 sample according to Ref. [19].

position [cm^{-1}]	label	assignment
3576	OH^-	stretching vibration due to crystalline OH^-
1098	ν_3	triply degenerated anti-symmetric P–O stretching mode
1037		
967	ν_1	non-degenerated symmetric P–O stretching mode
637	OH^-	bending vibration due to crystalline OH^-
608	ν_4	triply degenerated O–P–O bending mode
570		
477	ν_2	double degenerated bending mode of the O–P–O bond

Table 3
Average particle length and width of undoped and Nd^{3+}-Yb^{3+} doped HA NPs as calculated from TEM images.

	particle length	particle width
sample	[nm]	
Ca100	150 ± 29	25 ± 6
2 Yb:2Nd:Ca100	109 ± 37	15 ± 4
Sr75	105 ± 26	17 ± 4
2 Yb:2Nd:Sr75	100 ± 20	17 ± 4

ascribed to the formation of diffuse excitons after laser irradiation and their dissociation in proximity of the Yb^{3+} centers, that results in a subsequent radiative decay at the characteristic wavelength of the Yb^{3+}. When HA is doped by both Yb^{3+} and Nd^{3+} ions (see green curve), it can be found that Nd^{3+} strongly emits at 1060 and 1071 nm according to the $^4F_{3/2} \rightarrow {}^4I_{11/2}$ transition. Furthermore, a pronounced Yb^{3+} emission is detected at 980 nm, corresponding to the $^2F_{5/2} \rightarrow {}^2F_{7/2}$ transition. It is evident that the intensity of the Yb^{3+} emission at 980 nm is about 30 times higher than without Nd^{3+} co-doping, which is not only due to diffuse laser excitation, but Yb^{3+} ions are effectively pumped by the resonant energy transfer from Nd^{3+} centers. The transfer is even more efficient with Sr75 as matrix (red curve), with an Yb^{3+} emission intensity that is ~30% more intense than the one of 1.5 Yb:1.5Nd:Ca100. Considering the higher ionic radius of the Sr^{2+} ions with respect to the Ca^{2+}, the higher efficiency can be due to two effects: 1) the presence of Sr^{2+} ions can induce a distortion of the electric field around the lanthanide centers, creating a higher emission efficiency, or 2) the Sr^{2+} substitution promotes the generation of defects such as oxygen vacancies making favorable the de-excitation of excitons close to the lanthanide sites.

4. Conclusions

In the present work, Nd^{3+}-Yb^{3+} doped calcium hydroxyapatite (HA) and strontium-substituted hydroxyapatite nanoparticles were successfully synthetized by means of chemical precipitation procedure in

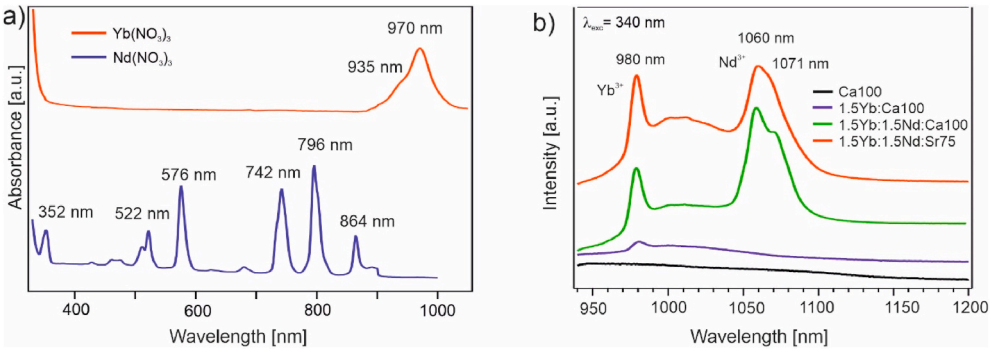

Fig. 3. (a) Absorbance spectra of $Yb(NO_3)_3$ and $Nd(NO_3)_3$ aqueous precursor solutions (0.045 M). (**b**) PL emission spectra of undoped and Nd^{3+}-Yb^{3+} doped HA samples under the excitation wavelength $\lambda = 340$ nm.

aqueous media.

Structural analyses (FT-IR and XRD) indicate that Nd^{3+} and Yb^{3+} ions successfully substitute Ca^{2+}/Sr^{2+} ions, without affecting the HA crystal structure in a significant way. The PL emission spectra reveal that the intensity of the Yb^{3+} ions' $^2F_{5/2} \rightarrow {}^2F_{7/2}$ optical transition at 980 nm is effectively enhanced by the energy transfer from Nd^{3+} ions, whose presence allow to obtain much greater emissions as compared to bare Yb^{3+} doping. Moreover, the energy transfer turns out to be even more efficient by adopting Sr-substituted HA NPs as matrix.

This study demonstrates that it is possible to effectively co-dope the HA structure with lanthanide ions and use the peculiar properties of specific donor-acceptor lanthanide couples (e.g. Nd^{3+} and Yb^{3+} in the specific case) to activate an efficient energy transfer process with a subsequent emission of light in a spectral region that in terms of energy (i.e. energy ~1.20 eV) makes these systems interesting for a wide range of applications, ranging from diagnostic imaging to photoactivated processes.

Funding

This research did not receive any specific grant from funding agencies in the public, commercial, or not-for-profit sectors.

CRediT authorship contribution statement

Marco Vittorio Nardi: Conceptualization, Methodology. **Melanie Timpel:** Conceptualization, Writing – original draftw, Writing – review & editingwand, Visualization. **Enrico Biondani:** Iinvestigation, Writing – original draftw, Visualization. **Riccardo Ceccato:** Iinvestigation, and, All authors have read and agreed to the published version of the manuscript. **Andrea Chiappini:** Vvalidation, Iinvestigation. **Sandra Dirè:** Methodology.

Declaration of competing interest

The authors declare that they have no known competing financial interests or personal relationships that could have appeared to influence the work reported in this paper.

Acknowledgments

The authors would like to thank Mr. Livio Zottele for the ICP-OES measurements and Dr. Gloria Ischia for the TEM measurements.

References

[1] J. Sona, G. Yia, J. Yooa, C. Parka, H. Kooa, H.S. Choi, Light-responsive nanomedicine for biophotonic imaging and targeted therapy, Adv. Drug Deliv. Rev. 138 (2019) 133–147, https://doi.org/10.1016/j.addr.2018.10.002.Light-Responsive.

[2] E.Z. Xu, C. Lee, S.D. Pritzl, A.S. Chen, T. Lohmueller, B.E. Cohen, E.M. Chan, P. J. Schuck, Infrared-to-ultraviolet upconverting nanoparticles for COVID-19-related disinfection applications, Opt. Mater. X. 12 (2021), https://doi.org/10.1016/j.omx.2021.100099.

[3] M. Adabi, M. Naghibzadeh, M. Adabi, M.A. Zarrinfard, S.S. Esnaashari, A. M. Seifalian, R. Faridi-Majidi, H. Tanimowo Aiyelabegan, H. Ghanbari, Biocompatibility and nanostructured materials: applications in nanomedicine, Artif. Cells, Nanomed. Biotechnol. 45 (2017) 833–842, https://doi.org/10.1080/21691401.2016.1178134.

[4] H. Dong, S.R. Du, X.Y. Zheng, G.M. Lyu, L.D. Sun, L.D. Li, P.Z. Zhang, C. Zhang, C. H. Yan, Lanthanide nanoparticles: from design toward bioimaging and therapy, Chem. Rev. 115 (2015) 10725–10815, https://doi.org/10.1021/acs.chemrev.5b00091.

[5] J. Hu, Y. Tang, A.H. Elmenoufy, H. Xu, Z. Cheng, X. Yang, Nanocomposite-based photodynamic therapy strategies for deep tumor treatment, Small 11 (2015) 5860–5887, https://doi.org/10.1002/smll.201501923.

[6] D.J. Naczynski, M.C. Tan, M. Zevon, B. Wall, J. Kohl, A. Kulesa, S. Chen, C.M. Roth, R.E. Riman, P.V. Moghe, Rare-earth-doped biological composites as in vivo shortwave infrared reporters, Nat. Commun. 4 (2013) 2199, https://doi.org/10.1038/ncomms3199.

[7] M. Mucalo (Ed.), Hydroxyapatite (HAp) for Biomedical Applications, Woodhead Publishing Series in Biomaterials, 2015, https://doi.org/10.1016/C2013-0-16440-9.

[8] A.S. Khan, A.A. Chaudhry, Handbook of Ionic Substituted Hydroxyapatites, Woodhead Publishing Series in Biomaterials, 2020. A volume.

[9] F.R.O. Silva, N.B. Lima, W.K. Yoshito, A.H.A. Bressiani, L. Gomes, Development of novel upconversion luminescent nanoparticle of Ytterbium/Thulium–doped beta tricalcium phosphate, J. Lumin. 187 (2017) 240–246, https://doi.org/10.1016/j.jlumin.2017.03.029.

[10] I.A. Neacsu, A.E. Stoica, B.S. Vasile, E. Andronescu, Luminescent hydroxyapatite doped with rare earth elements for biomedical applications, Nanomaterials 9 (2019), https://doi.org/10.3390/nano9020239.

[11] S. Mondal, V.T. Nguyen, S. Park, J. Choi, T.M. Thien Vo, J.H. Shin, Y.H. Kang, J. Oh, Rare earth element doped hydroxyapatite luminescent bioceramics contrast agent for enhanced biomedical imaging and therapeutic applications, Ceram. Int. 46 (2020) 29249–29260, https://doi.org/10.1016/j.ceramint.2020.08.099.

[12] Y.F. Wang, G.Y. Liu, L.D. Sun, J.W. Xiao, J.C. Zhou, C.H. Yan, Nd3+-sensitized upconversion nanophosphors: efficient in vivo bioimaging probes with minimized heating effect, ACS Nano 7 (2013) 7200–7206, https://doi.org/10.1021/nn402601d.

[13] F. Ai, Q. Ju, X. Zhang, X. Chen, F. Wang, G. Zhu, A core-shell-shell nanoplatform upconverting near-infrared light at 808 nm for luminescence imaging and photodynamic therapy of cancer, Sci. Rep. 5 (2015) 10785, https://doi.org/10.1038/srep10785.

[14] Y. Tai, X. Li, B. Pan, Efficient near-infrared down conversion in Nd3+-Yb3+ co-doped transparent nanostructured glass ceramics for photovoltaic application, J. Lumin. 195 (2018) 102–108, https://doi.org/10.1016/j.jlumin.2017.10.051.

[15] M. Frasnelli, F. Cristofaro, V.M. Sglavo, S. Dirè, E. Callone, R. Ceccato, G. Bruni, A. Icaro Cornaglia, L. Visai, Synthesis and characterization of strontium-substituted hydroxyapatite nanoparticles for bone regeneration, Mater. Sci. Eng. C 71 (2017) 653–662, https://doi.org/10.1016/j.msec.2016.10.047.

[16] A. Bigi, E. Boanini, C. Capuccini, M. Gazzano, Strontium-substituted hydroxyapatite nanocrystals, Inorg. Chim. Acta. 360 (2007) 1009–1016, https://doi.org/10.1016/j.ica.2006.07.074.

[17] P.H. Yanti, N. Nia, The effect of pH on synthesis of hydroxyapatite from geloina coaxans shell, IPTEK J. Proc. Ser. 3 (2017) 33–38.

[18] L. Lutterotti, Maud: a Rietveld analysis program designed for the internet and experiment integration, Acta Crystallogr. Sect. A Found. Crystallogr. 56 (2000) s54, https://doi.org/10.1107/S0108767300021954.

[19] S. Koutsopoulos, Synthesis and characterization of hydroxyapatite crystals: a review study on the analytical methods, J. Biomed. Mater. Res. 62 (2002) 600–612, https://doi.org/10.1002/jbm.10280.

[20] C.S. Ciobanu, S.L. Iconaru, F. Massuyeau, L.V. Constantin, A. Costescu, D. Predoi, Synthesis, structure, and luminescent properties of europium-doped

hydroxyapatite nanocrystalline powders, J. Nanomater. (2012), https://doi.org/10.1155/2012/942801, 2012.
[21] J. Barralet, S. Best, W. Bonfield, Carbonate substitution in precipitated hydroxyapatite: an investigation into the effects of reaction temperature and bicarbonate ion concentration, J. Biomed. Mater. Res. 41 (1998) 79–86, https://doi.org/10.1002/(SICI)1097-4636(199807)41:1<79::AID-JBM10>3.0.CO;2-C.
[22] B.O. Fowler, Infrared studies of apatites. II. Preparation of normal and isotopically substituted calcium, strontium, and barium hydroxyapatites and spectra-structure-composition correlations, Inorg. Chem. 13 (1974) 207–214, https://doi.org/10.1021/ic50131a040.
[23] A. Kaflak, W. Kolodziejski, Complementary information on water and hydroxyl groups in nanocrystalline carbonated hydroxyapatites from TGA, NMR and IR measurements, J. Mol. Struct. 990 (2011) 263–270, https://doi.org/10.1016/j.molstruc.2011.01.056.
[24] X. Xie, N. Gao, R. Deng, Q. Sun, Q. Xu, X. Liu, Mechanistic investigation of photon upconversion in Nd(3+)-sensitized core-shell nanoparticles, J. Am. Chem. Soc. 135 (2013), https://doi.org/10.1021/ja4075002, 12608–11.